Energy & Environmental Science

Cite this: *Energy Environ. Sci.*, 2012, **5**, 9055

www.rsc.org/ees

**PAPER**

# Concentrated solar thermoelectric generators†

**Lauryn L. Baranowski,[a] G. Jeffrey Snyder[b] and Eric S. Toberer*[c]**

***Received 17th May 2012, Accepted 6th August 2012***
**DOI: 10.1039/c2ee22248e**



Solar thermoelectric generators (STEGs) are solid state heat engines that generate electricity from concentrated sunlight. In this paper, we develop a novel detailed balance model for STEGs and apply this model to both state-of-the-art and idealized materials. This model uses thermoelectric compatibility theory to provide analytic solutions to device efficiency in idealized materials with temperature-dependent properties. The results of this modeling allow us to predict maximum theoretical STEG efficiencies and suggest general design rules for STEGs. With today's materials, a STEG with an incident flux of 100 kW $m^{-2}$ and a hot side temperature of 1000 °C could achieve 15.9% generator efficiency, making STEGs competitive with concentrated solar power plants. Future developments will depend on materials that can provide higher operating temperatures or higher material efficiency. For example, a STEG with $zT = 2$ at 1500 °C would have an efficiency of 30.6%.

## Introduction

There are many technologies available to directly harness the sun's energy, the most prevalent of which are photovoltaics and solar thermal (also known as concentrated solar power). Solar thermal technologies produce electric power from a temperature gradient, traditionally by using conventional heat engines.[1] Solid state heat engines, in the form of thermoelectric generators (TEGs), can also exploit this temperature gradient to generate power.[2]

A thermoelectric (TE) material generates a voltage in response to a temperature gradient. The efficiency of a thermoelectric material is governed by its figure of merit, $zT$, defined as $zT = \frac{\alpha^2 T}{\kappa\rho}$, where $\alpha$ is the Seebeck coefficient, $\kappa$ the thermal conductivity, and $\rho$ the electrical resistivity. Until recently, thermoelectric materials had demonstrated peak $zT$ values of 0.5–0.8, leading to low conversion efficiencies and limiting these materials to niche applications.[3]

With the advent of nanostructured thermoelectrics and complex bulk materials in the 1990s, there has been a sharp increase in $zT$.[2,4–7] Fig. 1 shows advanced materials that exhibit $zT$ values well in excess of unity over a broad range of temperatures. These high performing materials have led to a record of 15% unicouple efficiency reported by the Jet Propulsion Laboratory in 2012.[8]

In light of these recent developments, we consider solar thermoelectric generators (STEGs). In this work, we concentrate our analysis on high efficiency, concentrated STEGs. STEGs have several advantages as compared to existing solar technologies. Unlike traditional solar thermal generators, STEGs are solid

[a]*Materials Science, Colorado School of Mines, Golden, CO 80401, USA*
[b]*Materials Science, California Institute of Technology, Pasadena, CA 91125, USA*
[c]*Department of Physics, Colorado School of Mines, Golden, CO 80401, USA. E-mail: etoberer@mines.edu*

† Electronic supplementary information (ESI) available. See DOI: 10.1039/c2ee22248e

### Broader context

Technologies that can directly harness the sun's energy are becoming increasingly important in today's energy landscape, the most prevalent of which are photovoltaics and solar thermal (also known as concentrated solar power, or CSP). Installed CSP plants, which use conventional heat engines to generate electric power from a temperature gradient, typically operate at 14–16% efficiency. Solar thermoelectric generators (STEGs), which are solid state heat engines, represent an alternative to traditional CSP. STEGs can operate at higher temperatures than CSP systems and do not require moving generator parts or working fluids. In this paper, we develop a detailed balance approach to deriving the maximum theoretical STEG efficiency. Our optimized STEG uses a solar selective absorber to efficiently capture the incident solar flux, while limiting radiative losses. We predict that a STEG made with today's materials ($zT = 1$) and a hot side temperature of 1000 °C could achieve an efficiency of 15.9% under illumination by 100 suns. With reasonable improvements in thermoelectric materials ($zT = 2$), we expect a limiting efficiency of 23.5% for the same hot side temperature and level of illumination.

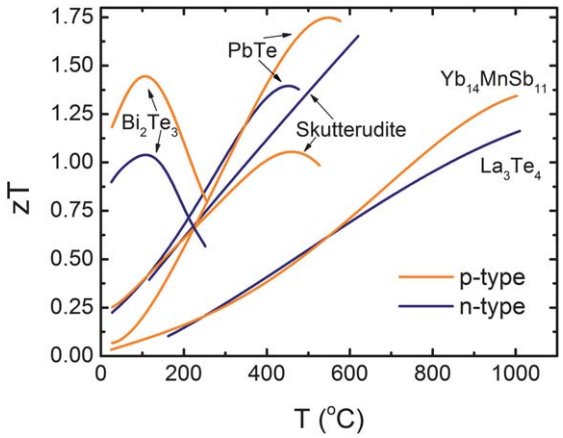


**Fig. 1** Advanced thermoelectric materials demonstrate $zT$ values well above 1, for both n- and p-type materials. This represents a distinct improvement over traditional materials, which possess peak $zT$ values between 0.5 and 0.8. Data from ref. 9–16.

state devices with no moving parts, which greatly increases reliability and lifetime. Additionally, STEGs are a scalable technology that can be used for small- or large-scale applications. While photovoltaics are limited to the fraction of incident solar radiation above the bandgap, STEGs utilize a larger portion of the solar spectrum.

### Basic STEG design

The TE efficiency within the STEG is defined as the ratio of the output electric work to the input heat. Like all heat engines, the efficiency of TEGs is limited by the Carnot efficiency. For a fixed cold side temperature ($T_c$), an increase in the hot side temperature ($T_h$) will result in a higher total efficiency of the thermoelectric generator. In order to achieve high values of $T_h$, we look to high levels of optical concentration, as well as optical and thermal concentration systems with high efficiencies.

The total efficiency of a STEG depends on the optical, absorber, and thermoelectric subsystem efficiencies. A STEG can be divided into several subsystems, as seen in Fig. 2a. The first is an optical system to concentrate the solar radiation. Second, a thermal absorber converts the incident light to heat, which then flows to the thermoelectric module. The cold side temperature of the TE is maintained by a passive or active cooling system. Finally, the thermal absorber, TE module, and cooling system are encapsulated in a vacuum enclosure to prevent conductive and convective heat losses to the air. The vacuum enclosure could be similar to those used in evacuated solar hot water systems, which are widely used and have demonstrated lifetimes greater than 15 years.[17]

Optical concentration systems for high efficiency STEGs would be the same as those used for concentrated photovoltaic or solar thermal applications.[1] These include Fresnel lenses, heliostats in conjunction with a central receiver system, and parabolic dishes and troughs. For use in a STEG, the pertinent characteristics are the level of concentration reached, the tracking system required, and the optical efficiency.

The optical concentration ratio is defined as the ratio of the optical concentrator area (*i.e.*, the area of the lens or mirror that receives the incident light) to the absorber area upon which the

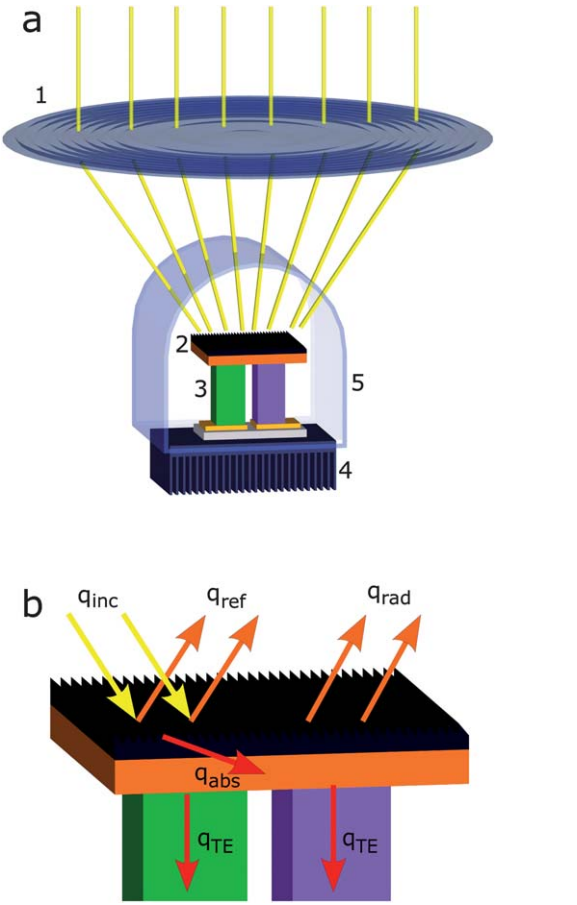


**Fig. 2** (a): A STEG can be broken down into five subsystems. (1) Optical concentration. (2) Thermal absorber. (3) Thermoelectric module. (4) Cooling system. (5) Vacuum encapsulation. (b) Energy incident upon the selective absorber ($q_{inc}$) is either absorbed ($q_{abs}$) or reflected ($q_{ref}$). Some of the absorbed energy is re-radiated to the atmosphere ($q_{rad}$), and the rest is transferred to the TE ($q_{TE}$). Radiation insulation to prevent heat loss on the back side of the absorber is not shown.

light is focused. Considering one sun to be approximately 1 kW $m^{-2}$, the flux after concentration is given by this solar flux multiplied by the optical concentration ratio. The concentration ratio is mainly limited by the type of solar tracking used. For a static concentrator, with no tracking, the optical concentration ratio is limited to about 10. When single-axis tracking is introduced, a concentration ratio of 100 can be achieved, above which dual-axis tracking systems are required.[18]

The optical efficiency is the ratio of light that reaches the absorber to the total light incident upon the optical concentrator, and increases with improved tracking systems. Typical optical efficiencies are 40% for static concentrators, 60% for single-axis tracking, and 85–90% for dual-axis tracking.[19] With dual-axis tracking, the optical losses of the tracking system itself are very low; other losses due to factors such as soiling of the lens surface, reflection, and absorption are still present.[20] It is also important to remember that increased tracking increases the system cost.

In order for the thermal absorber to effectively convert the incident light to heat, the surface must have a high absorptivity. However, by Kirchhoff's Law, this also invokes a high emissivity, leading to large radiative losses. This conflict can be

 

resolved by the use of a selective absorber, which has energy dependent absorptivity/emissivity. As can be seen in Fig. 3, the incident solar flux and the black body emission spectrum peak at different energies. In an ideal selective absorber, the absorptivity takes the form of a step function, in which the step from zero to one is located between the black body and solar flux maxima. The location of the step-edge is referred to as the cutoff energy.[21] This optimum cutoff energy is a function of both temperature and optical concentration.

Materials such as semiconductors are often considered intrinsic absorbers, meaning that they exhibit some solar selectivity as pure materials.[22] For a semiconductor, the cutoff value between high and low absorptivities is determined by the bandgap of the material. In recent years, intrinsic absorbers have been used as the starting materials for high performing selective absorbers, ranging from simple layered designs to highly sophisticated plasmonic and photonic structures.[22–24] High temperature absorbers (above 750 °C) have been developed that exhibit solar absorptivities above 0.8 and thermal emissivities below 0.15.[21,25]

## Previous work

The first documented STEG design dates from 1888, when Weston patented a device that concentrated solar radiation onto a thermoelectric module with a black absorber surface.[26,27] Subsequently, Severy described a STEG that included a pump to supply cooling water to the cold side of the TE module, a battery to store the generated electrical energy, and an adjustable tracking device.[28,29] In 1913, Coblentz published the first experimental results for a STEG with a hot side temperature of 100 °C.[30] However, Coblentz did not give an experimental efficiency for his device.

In 1954, Maria Telkes reported the first experimental STEG efficiency using flat-plate collectors in combination with a ZnSb/BiSb thermocouple. This device demonstrated 0.6% efficiency, which increased to 3.4% when a 50-fold concentrating lens was added.[31] After this initial study, experimental STEG work was intermittent, with low efficiency values due to relatively low hot side temperatures and the lack of vacuum encapsulation to prevent convective losses. Telkes' 1954 results were not surpassed until 2011, when Kraemer *et al.* experimentally demonstrated

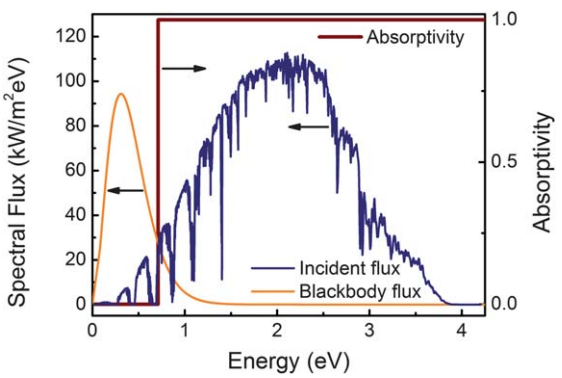


**Fig. 3** A selective absorber can be used to maximize the flux absorbed and minimize the flux re-radiated to the atmosphere. Here, the optimized energy cutoff is shown for a direct incident flux of 200 kW $m^{-2}$ and a black body temperature of 1000 °C.

4.6% efficiency in a $Bi_2Te_3$ nanostructured STEG.[32] Important features of this design included a selective absorber as a thermal concentrator and the use of a vacuum enclosure to minimize conductive and convective losses. A summary of the experimental results to date is shown in Table S1 of the ESI.†

The modeling of STEGs is complicated by the multitude of subsystems, such as the optical and thermal concentrators, as well as the challenges inherent in the modeling of thermoelectric generators. Thus far, all models have used the constant property model (CPM) to treat the performance of the TE, in which the transport properties of the TE (Seebeck coefficient and thermal and electrical conductivities) are assumed to be constant with temperature. This approach is reasonable for small $\Delta T$ across the device, but breaks down when larger $\Delta T$s are used. Real TE materials have properties which depend strongly on temperature. When modeling STEGs, it can be difficult to determine which variables (Table 1) or effects are significant, and thus the modeling results in the literature vary widely.

Along with her experimental work, Telkes developed a thermodynamic model for low temperature STEGs with no solar concentration.[31] In the latter half of the 20th century, other thermodynamic STEG models were occasionally developed.[33,34] Notably, in 1979, high temperature STEGs were considered using SiGe thermoelectric elements with a hot side temperature of 827 °C and 100-fold optical concentration to predict efficiencies around 12%.[35] In 2003, Scherrer *et al.* used the idea of thermal concentration to decrease the amount of TE material required. This study found that there was an optimum thermal concentration above which radiative losses from the large absorber surface reduced the total efficiency.[36] Around the same time, several studies were published that attempted to geometrically optimize the TE module for maximum STEG performance.[37–39]

In 2011, a paper by G. Chen modeled STEGs using a thorough CPM approach to highlight the important design variables. In this paper, Chen advocated for increasing the efficiency of the STEG by using a selective absorber to maximize the net flux into the thermal concentrator. Chen predicted that STEG efficiencies of approximately 12% can be achieved with 10-fold optical concentration and 200-fold thermal concentration, for a module

**Table 1** Variables

| Symbol | Definition |
|---|---|
| $T_h$ | TE hot side temperature |
| $T_{abs}$ | Temperature of the absorber surface |
| $\gamma_{th}$ | Thermal concentration |
| $\eta_{op}$ | Optical efficiency |
| $\eta_{abs}$ | Absorber efficiency |
| $\eta_{TE}$ | Thermoelectric efficiency |
| $\eta_{STEG}$ | STEG efficiency, $\eta_{abs} \cdot \eta_{TE}$ |
| $q_{inc}(E)$ | Spectral energy flux incident on the absorber surface |
| $q_{ref}(E)$ | Spectral energy flux reflected from absorber surface |
| $q_{abs}$ | Heat absorbed by the absorber surface |
| $q_{TE,in}$ | Heat transferred to the TE leg |
| $q_{rad}$ | Heat lost radiatively from the absorber surface |
| $q_{bb}(E)$ | Spectral black body emission flux |
| $A_{abs}$ | Area of the absorber surface |
| $A_{TE}$ | Area of the TE leg |
| $l_{TE}$ | Length of the TE leg |
| $\kappa_{eff}$ | TE effective thermal conductivity |
| $L_{th}$ | Thermal length, $\gamma_{th} l_{TE}$ |

operating at 527 °C with an average $zT$ of 1.[17] Following shortly thereafter, a paper by McEnaney *et al.* modeled segmented and cascaded $Bi_2Te_3$/skutterudite STEGs, using data from currently existing thermoelectric materials and selective surfaces. The efficiency of the cascaded design was predicted to be the highest, reaching 16% at 600 °C.[40] While this study did much to shed light on the important design variables of a STEG, the predicted device performance was determined by finite element modeling for a specific generator design and TE materials. Thus to date, STEG modeling efforts have been numerical approaches or have used CPM to address TE performance, limiting the applicability of these models.

In this study, we develop a generalized description of STEGs that is analytic and is not limited by CPM. We consider optimized TE geometries, selective absorbers, and total efficiencies for given optical and thermal concentrations. This global optimization is done from the view of a fixed hot side temperature, because of the inherent temperature limits of TE materials. We finish by using advanced TE materials' experimental data to design an optimized STEG module.

## Methods

In deriving the total system efficiency, we separate the optical efficiency from the STEG efficiency. The STEG can be broken down into two subsystems: the thermal absorber and the TEG. The efficiency for each subsystem can be derived individually, and the STEG efficiency is simply the product of the two. The absorber efficiency is defined as the ratio of the heat transferred to the TE to the total heat that strikes the absorber surface. We must first consider the modeling of the selective absorber to determine how much of this incident heat is actually absorbed by the surface. Then, the absorber efficiency is derived using heat transfer modeling to consider the conductive and radiative heat flows within the absorber and the TE leg. The thermoelectric efficiency is derived for model materials with a temperature independent $zT$ and for real materials in a cascaded generator.

### Heat transfer modeling

In the following thermodynamic analysis, we can define spectral heat fluxes, which represent power per unit area per unit energy, total heat fluxes, which represent power per unit area, and heat rates, which represent energy per unit time (power). In the following sections, spectral heat fluxes are represented by $q''(E)$, and have units of kW m$^{-2}$ eV$^{-1}$ and total heat fluxes will be represented by $q''$ and are in units of kW m$^{-2}$. Heat rates will be represented by $q'$ in units of kW. Integration of the spectral heat flux gives the total heat flux: $q'' = \int q''(E)dE$. The total heat flux and the heat rate can be related to each other through the area of the surface in question, so that $q = q''A$. The pertinent heat rates for the system are shown in Fig. 2b.

**Table 2** Fixed parameters

| Symbol | Definition | Value |
|---|---|---|
| $T_c$ | TE cold side temperature | 100 °C |
| $q''_{sun}(E)$ | Spectral solar energy flux | AM 1.5 direct spectrum (scaled) |
| $\alpha_s(E)$ | Spectral absorptivity | 1, $E$ > cutoff energy, 0 otherwise |
| $zT$ | TE figure of merit | 1, 2 |
| $\kappa_{TE}$ | TE thermal conductivity | 1 W m$^{-1}$ K$^{-1}$ |

After passing through the optical concentration system, the concentrated solar flux is transmitted through the vacuum enclosure and is incident upon the surface of the absorber ($q''_{inc}$). Here, the spectral solar flux ($q''_{sun}(E)$) is given by the AM 1.5 direct spectrum (version G173-03), which yields 0.9 kW m$^{-2}$ when integrated over the entire spectrum (Table 2). This solar flux is concentrated by the optical system to give a final value of $q''_{inc}(E)$.

An ideal selective absorber is a material in which the absorptivity exhibits a step edge between zero and one at a specific value of energy referred to as the cutoff energy (an example of this function can be seen in Fig. 3). We define the optimal cutoff energy as that which results in the highest net flux into the absorber ($q''_{abs} - q''_{rad}$). As the energy cutoff is a function of both the absorber temperature and the incident flux, we iteratively determine an optimum energy cutoff for each combination of these variables.

The absorber surface is not a perfect black body, and thus only a fraction of the incident energy is absorbed ($q''_{abs}$) and the remainder is reflected back into the atmosphere ($q''_{ref}$). The energy absorbed by the surface can be related to the total incident energy as:

$$q_{abs} = A_{abs}\int_0^\infty \alpha_s(E)q''_{inc}(E)dE \quad (1)$$

where $\alpha_s(E)$ is the spectral absorptivity, and $A_{abs}$ is the area of the absorber surface. Here, integration over all energies gives the total value of $q_{abs}$. This expression, as well as the following expression for the radiative heat loss (eqn (4)), is based on the same detailed balance principle that is used to calculate the maximum efficiency of photovoltaic devices.[41]

To consider the heat flow within the absorber, we assume the STEG is sufficiently well-designed that some losses may be neglected in our heat balance. First, we expect that the heat lost through convection will be minimal by enclosing the absorber and thermoelectric legs in a vacuum enclosure, as shown in Fig. 2a. Second, we assume design elements such as insulation and heat shielding are implemented to minimize the heat loss from the sides and back of the absorber. Finally, we assume a perfect selective absorber and neglect reflection losses in the absorbing region.

In this limit, the heat absorbed by the surface can either be re-radiated to the atmosphere ($q_{rad}$) or flow to the TE ($q_{TE,in}$), as shown in Fig. 2b. This can be represented by the following heat balance:

$$q_{abs} = q_{TE,in} + q_{rad} \quad (2)$$

We can then define the absorber efficiency as:

$$\eta_{abs} \equiv \frac{q_{TE,in}}{q_{inc}} = \frac{q_{abs} - q_{rad}}{q_{inc}} = \frac{q''_{abs} - q''_{rad}}{q''_{inc}} \quad (3)$$

Any heat which does not flow through the thermoelectric module is considered a parasitic loss.

Following Kirchhoff's law of thermal radiation ($\alpha(E) = \varepsilon(E)$), the radiative heat loss is calculated by integrating the product of the spectral emissivity and the black body emission spectrum:

$$q_{rad} = A_{abs}\pi \int_0^\infty \varepsilon_s(E) q''_{bb}(E) dE$$
$$q''_{bb}(E) = \frac{2E^3}{c^2 h^3} \frac{1}{e^{E/k_B T} - 1} \quad (4)$$

in which the factor of $\pi$ is the result of integration over a half-sphere.

Quantifying the radiative loss from the absorber *via* eqn (4) requires determining the temperature of the absorber surface ($T_{abs}$), which will differ from $T_h$. Because of the differences in magnitude of the thermal conductivity of the absorber (for example, ~55 W m$^{-1}$ K$^{-1}$ for graphite at 1000 °C [42]) and the TE (~1 W m$^{-1}$ K$^{-1}$), the temperature drop across the absorber will be very small compared to the drop across the TE. The difference between $T_{abs}$ and $T_h$ has been calculated, and is less than 0.5% for most of the variable space, with a maximum difference of 1.5% (see ESI†). We thus assume that $T_{abs} = T_h$, which greatly simplifies the STEG model. We have also assumed that there is no lateral temperature gradient across the absorber surface. If the absorber surface is sufficiently thermally conductive, then the lateral temperature change across the absorber is indeed minimal. This can be shown by calculating the temperature distribution over a basic annular fin model, which has been done by Kraemer *et al.*[32] We have also performed this calculation for our system, and these data are presented in the ESI.†

We can express the conductive heat transfer into a TE leg of area $A_{TE}$ and length $l_{TE}$ as:

$$q_{TE,in} = (T_h - T_c) \frac{\kappa_{eff} A_{TE}}{l_{TE}} \quad (5)$$

In a thermoelectric material, the heat balance is complicated by the Joule and Thomson effects. While there is significant heat divergence within a thermoelectric leg ($q_{TE,in} \neq q_{TE,out}$), here we are only concerned with the heat flux entering the leg from the absorber. In the Appendix, we develop an expression for heat transfer into the thermoelectric leg in terms of an effective thermal conductivity ($\kappa_{eff}$, eqn (A.20)). This model rigorously considers the Joule and Thomson effects in the leg and allows these terms to be included within a simple Fourier law description of conduction (eqn (5)). To our knowledge, this concept of effective thermal conductivity in thermoelectrics has not been considered before.

The absorber efficiency (eqn (3)) describes the ratio of the heat transferred to the TE leg ($q_{TE}$) to the total heat incident upon the absorber ($q_{inc}$). Thus, the value of the absorber efficiency can be used to quantify the reflective and radiative losses of the system. Using our definition of the incident flux, in combination with eqn (5), yields:

$$\eta_{abs} = \frac{(T_h - T_c)\kappa_{eff} A_{TE}}{q''_{inc} A_{abs} l_{TE}} \quad (6)$$

Rather than considering the areas of both the absorber and the TE, it is simpler to consider the ratio of the two, defined as the thermal concentration ($\gamma_{th}$):

$$\gamma_{th} \equiv \frac{A_{abs}}{A_{TE}} \quad (7)$$

We thus obtain an expression for $\eta_{abs}$ which depends on two geometric parameters: $l_{TE}$ and $\gamma_{th}$. To simplify our optimization, we define a "thermal length": $L_{th} \equiv \gamma_{th} \cdot l_{TE}$. Conveniently, an expression for $L_{th}$ can be developed by combining eqn (3) and (6):

$$L_{th} = \frac{(T_h - T_c)\kappa_{eff}}{q''_{abs} - q''_{rad}} \quad (8)$$

The numerical value of $L_{th}$ results from the maximization of the net flux ($q''_{abs} - q''_{rad}$) for a given $q''_{inc}$ and $T_h$. This is done *via* the energy cutoff, and yields an optimized absorber efficiency. The remaining parameters in eqn (8) ($T_c$ and $\kappa_{eff}$) are chosen to be 100 °C and determined using eqn (A.20), respectively (Table 2). Thus, the $L_{th}$ value is an optimized length and not a free parameter.

### Thermoelectric efficiency

The efficiency of thermoelectric generators has traditionally been analyzed using the constant property model (CPM), a global approach to the transport properties.[43,44] Recently, a local approach to generator efficiency has been developed which greatly simplifies the analysis and optimization. This approach is derived in ref. 45 and 46; here we review the key features.

This local approach differs from the CPM in that it does not inherently assume any material properties. Because of the lack of assumptions in this model, it is necessary to constrain some parameters in order to reach an analytical solution. Here, we assume constant thermal conductivity and $zT$. For many TE materials, the $\kappa_{TE}$ value varies by less than 50% over a several hundred degrees temperature range (see, for example, the $\kappa_{TE}$ data in ref. 9–16). In contrast, the Seebeck coefficient and electrical conductivity often vary by several orders of magnitude over the same temperature range. Cascaded and segmented generator designs allow for an approximately constant value of $zT$.

The macroscopic thermoelectric leg is infinitely divided into layers which are electrically and thermally in series. The maximum local efficiency is set by the local Carnot efficiency $dT/T$. In practice, the local efficiency is a fraction of $dT/T$; this fraction is termed the reduced efficiency $\eta_r(T)$. Thus an ideal Carnot generator would have an $\eta_r(T)$ of unity for all $T$. Given $\eta_r(T)$ across a leg, the global efficiency can be derived:

$$\eta_{TE} = 1 - \exp\left( - \int_{T_c}^{T_h} \frac{\eta_r}{T} dT \right) \quad (9)$$

We will pursue two approaches, the first with generalized material properties and the second specific to the current state-of-the-art materials. In both cases, prediction of optimum performance requires an optimized reduced current density $u$. In a thermoelectric leg, the reduced current density can be defined as the ratio of the electric current density, $J$, to the heat flux by conduction, $\kappa \nabla T$.

$$u \equiv \frac{J}{\kappa \nabla T} \quad (10)$$

For a constant $\kappa \nabla T$, we can see that $u$ is simply a scaled version of the current density $J$.

The local reduced efficiency is found to be:

$$\eta_r(T) = \frac{u(\alpha - \rho\kappa u)}{u\alpha + \frac{1}{T}} \quad (11)$$

By tuning the reduced current density $u$, $\eta_r$ can be maximized. The peak in $\eta_r$ occurs when $u$ is equal to the 'thermoelectric compatibility factor' $s$, which is defined as:

$$s \equiv \frac{\sqrt{1+zT}-1}{\alpha T} \tag{12}$$

The maximum reduced efficiency, obtained when $u = s$, is given by

$$\eta_{r,max} = \frac{\sqrt{1+zT}-1}{\sqrt{1+zT}+1} \tag{13}$$

As a general rule, $\eta_r(T)$ is significantly compromised when $u$ deviates from $s$ by more than a factor of two.

In our first approach, we assume that $u = s$ across the device. Cascading allows $u$ to be reset throughout the legs, enabling a real device to come close (within a factor of two) to $u = s$ at all $T$. As can be seen in eqn (13), the temperature dependence of $zT$ will be important in evaluating eqn (9). In a cascaded generator, the real temperature dependence of $zT$ will have a sawtooth appearance. Here we approximate $zT$ as a constant. If $zT$ is constant, then the reduced efficiency is also constant, and the integral in eqn (9) becomes trivial. With these assumptions, the global efficiency can be solved to yield:

$$\eta_{TE} = 1 - \left(\frac{T_c}{T_h}\right)^{\eta_{r,max}} \tag{14}$$

The second approach considers a cascaded STEG constructed from state-of-the-art thermoelectric materials with experimentally determined $\alpha(T)$, $\rho(T)$ and $\kappa(T)$ (and thus $zT(T)$). The interface temperatures between stages are set to maximize $zT$ values. In practice, this typically is the maximum temperature the lower temperature stage can sustain. This approach maximizes $\eta$ for a segment with a given $s(T)$ by iteratively determining the optimum $u(T)$. The efficiency $\eta$ is related to the change in thermoelectric potential ($\Phi$) across the device:

$$\eta = \frac{\Phi_h - \Phi_c}{\Phi_h} \tag{15}$$

The thermoelectric potential is defined as:[46]

$$\Phi(T) = (\alpha T + 1/u) \tag{16}$$

The heat balance equation can be expressed in reduced form:

$$\frac{du}{dT} = u^2 T \frac{d\alpha}{dT} + u^3 \rho\kappa \tag{17}$$

This governing expression determines the form of $u(T)$. The boundary condition for $u(T)$ is iteratively determined to maximize the global $\eta$.

### Overall STEG efficiency

The efficiency of the STEG is given by the product of the absorber and thermoelectric efficiencies ($\eta_{STEG} = \eta_{abs} \cdot \eta_{TE}$). It is important to note that we are not including the efficiency of the optical concentrating system within our value of the STEG efficiency. This is done to enable more direct comparisons to other solar energy devices, such as photovoltaics, for which the reported efficiencies do not include optical concentration losses.

In the approximation of constant $zT$ and $u = s$, this yields a simple expression for STEG efficiency:

$$\eta_{STEG} = \frac{q''_{abs} - q''_{rad}}{q''_{inc}} \left(1 - \left(\frac{T_c}{T_h}\right)^{\eta_r}\right) \tag{18}$$

The absorber efficiency can also be rewritten in terms of the physical system design parameters (as in eqn (6)). This gives us an alternate expression for the STEG efficiency.

$$\eta_{STEG} = \frac{(T_h - T_c)\kappa_{eff}}{q''_{inc} L_{th}} \left(1 - \left(\frac{T_c}{T_h}\right)^{\eta_r}\right) \tag{19}$$

In the case of a black body (for which the absorptivity is unity across all energies), the integrals in eqn (1) and (4) become trivial, and eqn (18) can be written as:

$$\eta_{STEG} = \frac{q''_{inc} - \sigma T_h^4}{q''_{inc}} \left(1 - \left(\frac{T_c}{T_h}\right)^{\eta_r}\right) \tag{20}$$

where $\sigma$ is the Stefan–Boltzmann constant. We emphasize that the choice of constant $zT$ is to provide analytic solutions within this paper; a numerical approach can be readily implemented to solve eqn (13) and (14) and is demonstrated below.

## Results and discussion

### Selective absorber results

In a selective absorber, the absorption cutoff is positioned to maximize the energy absorbed and minimize the radiative losses (shown in Fig. 3). The results of the selective absorber optimization performed here are shown in Fig. 4a. With an increase in temperature, the black body emission spectrum shifts to higher energies. To avoid high radiative losses in this situation, the cutoff also shifts to higher energy values. Conversely, as the incident solar flux increases, the magnitude of this incident flux becomes much larger than the black body emission curve. This moves the cutoff to lower energies, so as to absorb more of the concentrated solar flux. In all curves, we see sharp jumps in the energy cutoff values, which can be explained by considering the water absorption bands in the AM 1.5 spectrum (see Fig. 3). Because the incident flux is much lower within these bands, the total flux is decreased when the cutoff is positioned within an absorption band. The optimized cutoff will remain at an energy just below the absorption band, even as the temperature increases and the black body emission spectrum shifts to high energies, until it becomes advantageous for the cutoff to "jump" to the other side of the absorption band.

Because the use of a selective absorber increases both the cost and complexity of the STEG, one could also consider using a black body as the thermal absorber. Fig. 4b compares the ratio of the net flux achieved by the black body ($\phi_{BB} = q''_{abs} - q''_{rad}$) to the net flux achieved with an optimized selective absorber ($\phi_{SA}$). The difference between the black body and selective absorber fluxes is greatest at high temperatures and low incident fluxes. Because the radiative losses of the system show a $T_h^4$ dependence, the selective absorber is necessary to prevent large radiative losses at high temperatures. At low incident fluxes, the magnitudes of the incident and radiative fluxes are similar, and again a selective absorber is necessary to prevent large radiative losses. In contrast, at high incident fluxes the magnitude of the incident flux dwarfs that of the radiative flux, and the difference between the black body and selective absorber is less pronounced.



 

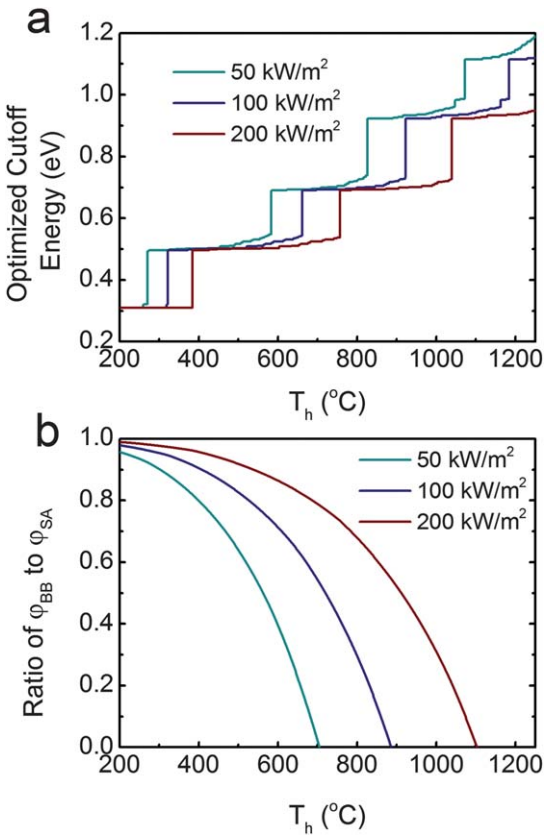


**Fig. 4** (a): The cutoff energy for a selective absorber must be optimized with respect to both temperature and optical concentration to achieve the maximum net flux into the absorber. The sharp jumps in this optimized value are due to the water absorption bands in the AM 1.5 spectrum. (b) When considering the net flux for a black body absorber ($\phi_{BB}$) *versus* the net flux for an optimized selective absorber ($\phi_{SA}$), the performance of the SA is markedly better at high temperatures and low incident fluxes.

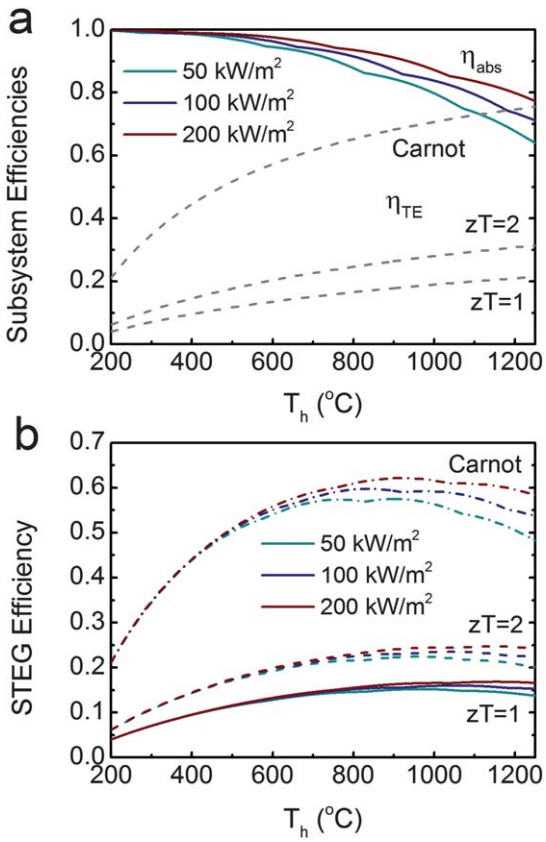


**Fig. 5** (a) Thermoelectric and absorber subsystem efficiencies, showing opposing trends with temperature. (b) The STEG efficiency, which is the product of the thermoelectric and absorber efficiencies.

### Subsystem efficiencies

We first consider the subsystem efficiencies derived above (eqn (6), (13) and (14)) as functions of temperature, shown in Fig. 5a. The thermoelectric and absorber efficiencies show opposing trends with temperature. As can be seen in eqn (14), the thermoelectric efficiency increases with increasing $T_h$. Increasing the $zT$ of the TE module also increases the thermoelectric efficiency (see eqn (13)), and the Carnot efficiency shows the highest possible efficiency for an ideal heat engine. In contrast, the absorber efficiency (eqn (6)) decreases with increasing $T_h$, due to the dependence of the radiative losses on $T_h$ (as shown in eqn (4)).

### STEG efficiency

Fig. 5b shows the STEG efficiency as a function of $T_h$, which is simply the product of the two subsystem efficiencies. Over the temperature region shown, the decrease in absorber efficiency is overshadowed by the increase in TE efficiency, resulting in an overall increase in the STEG efficiency. However, at higher temperatures, the STEG efficiency will exhibit a maximum value at a specific temperature (see Fig. 9). With the increasing incident flux, this maximum efficiency shifts to higher temperatures.

The $L_{th}$ value, given in eqn (8), represents the thermal resistance of the TE element. For a constant absorber area, an increase in $L_{th}$ requires either a decrease in $A_{TE}$ or an increase in $l_{TE}$, both of which increase the resistance to heat flow through the TE. In Fig. 6, the positive slope of $L_{th}$ as a function of $T_h$ is due to the increased thermal resistance necessary to achieve higher temperatures. At lower incident fluxes, a higher $L_{th}$ value is required: with a lower incident heat flux, the TE must be more

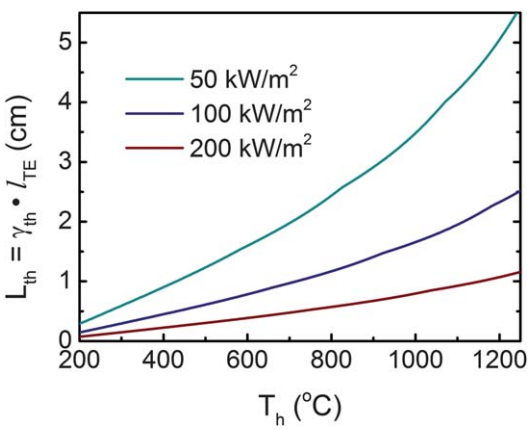


**Fig. 6** The $L_{th}$ value of the system, representing the thermal resistance of the TE element, increases with temperature. At lower incident fluxes, the TE must be more thermally resistive (higher $L_{th}$) to maintain a given value of $T_h$ (shown for $zT = 1$).

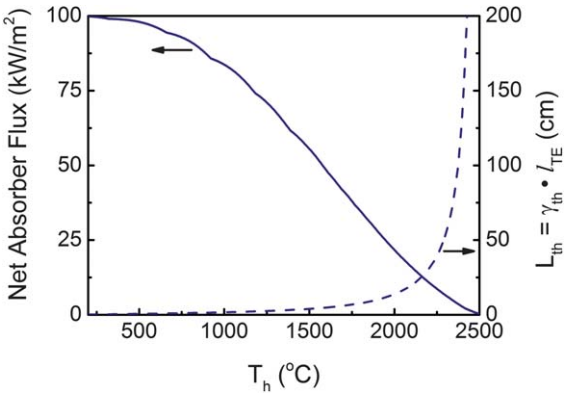


**Fig. 7** For a given incident flux, there is a maximum hot side temperature that the system can achieve. No heat can flow to the TE in this situation, because the thermal resistance ($l_{th}$) of the TE leg is infinite. At this temperature, the absorber efficiency (and thus the STEG efficiency) is zero (shown for $q''_{inc} = 100$ kW m$^{-2}$ and $zT = 1$).

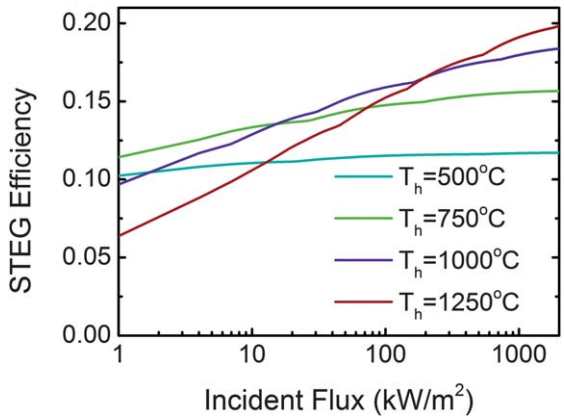


**Fig. 8** When $T_h$ is fixed and the incident flux is increased, the STEG efficiency will asymptote to a particular value. This asymptotic behavior is due to the increased magnitude of the incident flux as compared to the fixed value of the radiative flux (shown for $zT = 1$).

thermally resistive to maintain the same $T_h$ value as a system with a higher incident heat flux (see Fig. 6).

Past the optimal $T_h$ value, the total efficiency decreases to zero. This behavior is understood by examining the net flux into the absorber, given by the difference between the absorbed and radiated heat fluxes, as shown in Fig. 7. The temperature at which the net absorber flux is zero is the same as the temperature for an absorber efficiency (and thus a STEG efficiency) of zero. This places a limit on the maximum temperature attainable for a given incident flux.

The limiting temperature can also be understood in terms of physical system parameters. If we consider an increase in $T_h$ at a constant incident flux, the $L_{th}$ value will necessarily increase also, as shown in Fig. 7. At the limiting temperature, $L_{th}$ approaches infinity, representing an infinite thermal resistance (physically due to either a very long TE leg or a very small TE area). An infinite thermal resistance would mean that no heat was flowing to the TE, which is indeed what is shown by the heat balance at this limiting temperature.

Fig. 8 shows the STEG efficiency as a function of the incident flux. For each value of $T_h$, there is an incident flux past which the efficiency gains are minimal. Because the TE efficiency is not affected by the change in the incident flux, this can again be understood in terms of the absorber efficiency. As the incident flux increases, this value becomes many orders of magnitude larger than the radiative losses of the system, causing the absorber efficiency to asymptote at a particular value. This is then reflected in the asymptotic behavior of the STEG efficiency. With increasing $T_h$, this point of diminishing returns shifts to higher values of incident flux, due to the changes in the slope of the absorber efficiency with the increasing incident flux.

## Total efficiency

The total system efficiency is separated into the STEG efficiency and the efficiency of the optical concentrating system. Here, we consider both single- and dual-axis optical tracking systems with efficiencies of 0.6 and 0.9, respectively.[19] We have set the optical efficiency to be temperature independent, thus including this value simply scales the STEG efficiency curve. Fig. 9 shows the efficiency for a system with an ideal optical concentrator, and realistic single/dual-axis tracking systems, for $zT = 1$ and $zT = 2$. For the STEG with $zT = 1$, under 100 kW m$^{-2}$ illumination, the STEG efficiency is 15.9%. If a realistic dual-axis tracking system is used ($\eta_{op} = 0.9$), then the total efficiency is 14.3%. If the average $zT$ value of the system increases to 2, the STEG efficiency rises to 23.5%, and the total efficiency (with realistic dual-axis tracking) is 21.1%. Another material improvement that could

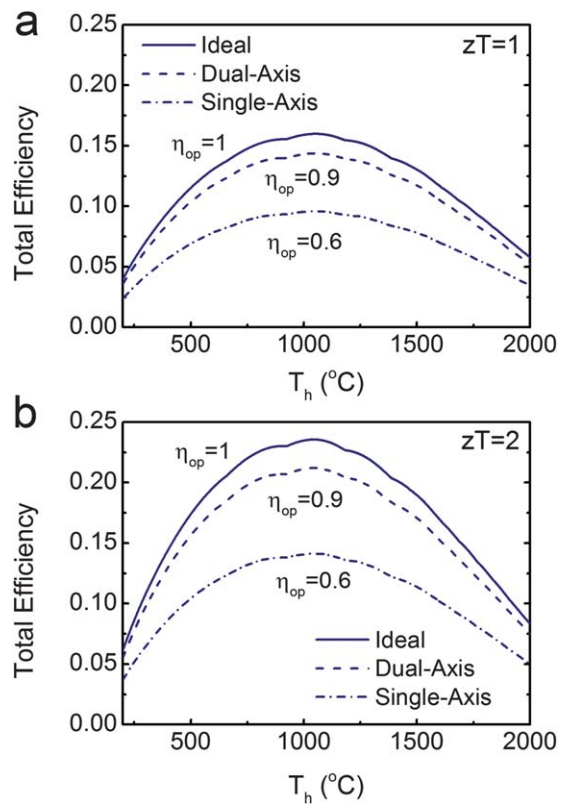


**Fig. 9** Total system efficiency for ideal and realistic optical concentration systems. The single- and dual-axis tracking systems have efficiencies of 0.6 and 0.9, respectively. In panel (a) the STEG has $zT = 1$, in panel (b) $zT = 2$ (shown for $q''_{inc} = 100$ kW m$^{-2}$).

increase the total efficiency is the development of higher temperature materials. For example, for a STEG with a hot side temperature of 1500 °C and a $zT$ value of 2, the STEG efficiency would be 30.6%, and the total efficiency 27.6% for a realistic dual-axis tracking system.

### Design elements of a STEG unit

After investigating the suite of variables that are involved in STEG design and optimization, it is illustrative to consider the physical design of an optimized STEG. We will consider each STEG subsystem individually, and discuss the materials required, their performance, and the system geometry.

We first consider the optical concentration system. If we choose to use a dual-axis tracking system, the most attractive choice is a Fresnel lens concentrator, which has been shown to have optical efficiencies of 85–90%. Acrylic Fresnel lenses are advantageous in that they are light, durable, and easily mass produced.[47]

From Fig. 4b, we see that the selective absorber performs markedly better than a black body absorber. In order to reach the high values of $T_h$ necessary for high efficiency STEGs, a selective absorber is required. High temperature selective absorbers have been designed that operate close to the limiting values considered here.[21,25]

We next discuss the choice of TE material and module design. We propose a cascaded design consisting of three individual TE stages. These are: (1) a $Bi_2Te_3$ stage from 100–247 °C, (2) a skutterudite stage from 247–527 °C, and (3) a $Yb_{14}MnSb_{11}$/$La_3Te_4$ stage from 527–1000 °C.[10,11,13–16] This design gives an effective $zT$ of 1.03 and an overall TE efficiency of 18.7%. For this same temperature range and $zT$, in the $u = s$ limit, our expression for $\eta_{TE}$ (eqn (14)) gives a value of 19.3% efficiency. We can further see that the actual TE module performance is very close to the theoretical performance by considering the $u$ and $s$ values of each section, shown in panels (a) and (b) of Fig. 10. In an individual stage, the difference between $u$ and $s$ is never more than a factor of two, not enough to adversely affect the generator performance. The impact of $u \neq s$ can be visualized throughout the leg in panels (c) and (d). The maximum reduced efficiency (pink) assumes $u = s$ and the local $zT$, whereas in the real device $u = s$ at only one point. Elsewhere, the pink (maximum) and green (actual) curves are not equal.

In order to consider the geometric parameters of the system, we first choose the dimensions of the TE leg. For the module optimization above, we have assumed that the TE leg length is 1 cm, and the total area is 1 $cm^2$ (the individual areas of the p- and n-type legs are optimized for each stage, but in all cases they sum to 1 $cm^2$). For a hot side temperature of 1000 °C and a 100 kW $m^{-2}$ incident flux, the $L_{th}$ value of the system is

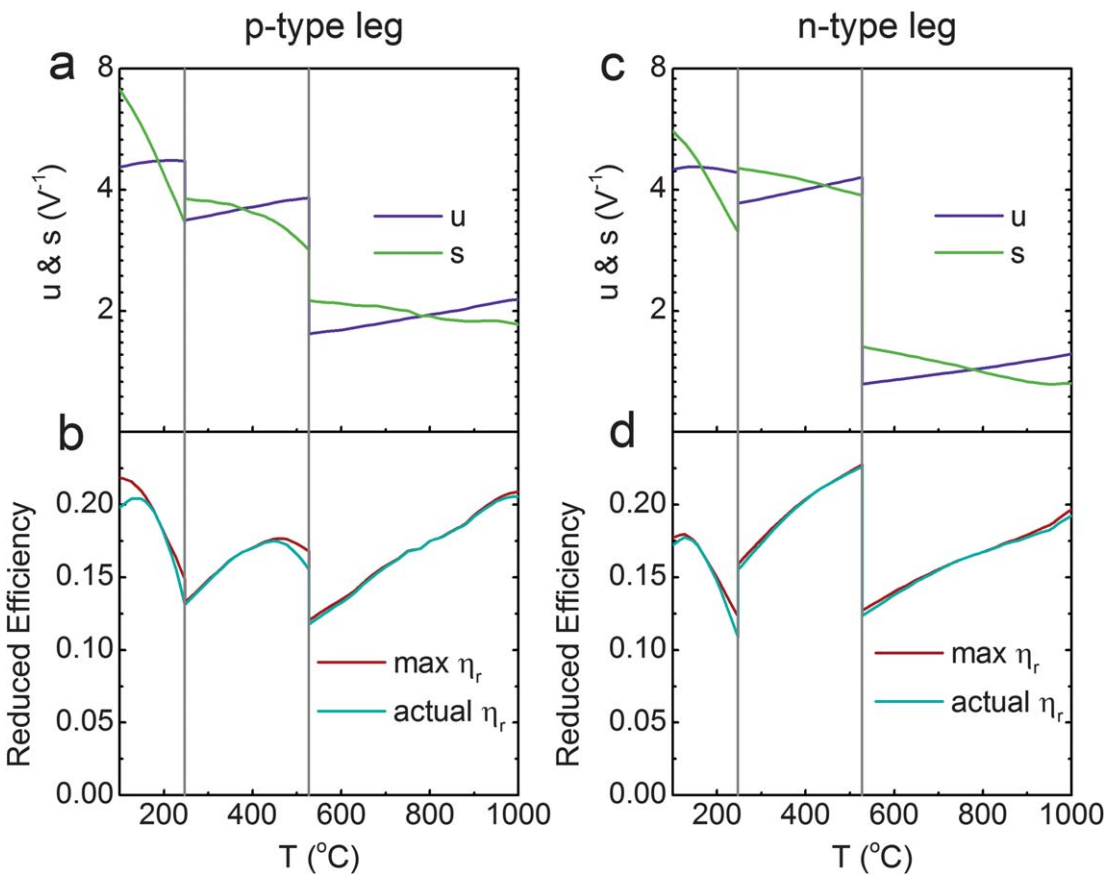


**Fig. 10** An optimized three-stage TE module using experimental data. By optimizing the reduced current density $u$, this value is never more than a factor of two different from the thermoelectric compatibility factor $s$. This allows the actual reduced efficiency of each stage to be close to the calculated maximum reduced efficiency.

approximately 1.6 cm. Using our TE dimensions, we calculate that the absorber area must be 1.6 $cm^2$. In practice, a STEG would consist of many of these 1 $cm^3$ thermoelectric units wired together, and the top side absorber would be continuous over the entire area.

For this design, the STEG efficiency is 15.7% when using an ideal optical concentration system that concentrates to 100 kW $m^{-2}$. If a realistic dual-axis tracking system is used, and this efficiency is taken into account ($\eta_{op} = 0.9$), the total efficiency is 14.1%.

### Comparison to other technologies

When the losses of the optical concentrating system are considered, we see that STEGs made from today's materials should achieve total system efficiencies around 14.1%. Concentrated solar power (CSP) systems, which use similar optical tracking and concentration systems, typically achieve about 13–15% system efficiency.[1] STEGs can clearly achieve comparable efficiencies, without the need for working fluids or moving generator parts. Additionally, the efficiency of STEGs has the potential to greatly increase in coming years, as TE materials with higher $zT$ values are developed. This is in contrast to CSP systems, which are already highly optimized. In a CSP system, the operating temperature is limited by the working fluid to a maximum of ~550 °C; we see from Fig. 9 that the optimal operating temperatures for STEGs are much higher.[1] This suggests the possibility of combining STEGs with CSP installations; the STEG could operate with a $T_c$ of 500 °C, leaving the CSP efficiency unchanged, while increasing the efficiency of the combined system.

Concentrated photovoltaics (CPVs) have a record efficiency of 43.5%, but in real operating conditions the efficiency is typically about 30%.[48] As noted above, if TE materials had an average $zT$ of 2, the STEG could in practice achieve a generator efficiency of 23.8% at $T_h = 1050$ °C (Fig. 9b).

CPV cells owe their record efficiencies to the use of multi-junctions, which simultaneously extends the range of wavelengths that can be absorbed by the cell and reduces thermalization losses. However, the traditional multi-junction arrangement presents some challenges, including lattice matching and limitations on the cell current. To avoid these, techniques which physically split the solar spectrum have been proposed, including photonic structures, reflective and refractive optics, and luminescent or holographic filters.[49,50] Although these techniques have been extensively modeled and experimentally demonstrated, much work remains before any spectrum splitting technology could be truly competitive with CPV.[51–54]

Ultimately, the value of any new technology is determined not only by efficiency but also by cost. The costs of CSP and PV plants are typically assessed by calculating the levelized cost of energy (LCOE).[55,56] However, this calculation is difficult for STEGs because module production costs are currently unknown. This is largely due to the fact that many of the high performing TE materials considered here have only recently been investigated in experimental settings. Only when these materials mature will it be possible to accurately calculate the LCOE for large scale STEG installations.

## Conclusions

We have developed a model that allows us to predict the limiting efficiency of a STEG. This has been achieved by separately optimizing the thermal absorber and the thermoelectric module using heat transfer modeling and thermoelectric compatibility theory, respectively. Our optimization has also allowed us to develop generalized design rules for STEGs. These can be used to inform STEG design choices, such as the level of optical concentration, the use of a selective absorber, and the thermal absorber and thermoelectric module geometries.

With current TE materials, we have shown that a total efficiency of 14.1% is possible with a hot side temperature of 1000 °C, including a non-ideal optical system. Solar thermal systems, which use similar optical tracking and concentration systems, typically achieve about 13–15% system efficiency. STEGs can clearly achieve comparable efficiencies, without the need for working fluids or moving generator parts. As TE materials continue to develop, STEG system efficiencies will increase; if the average $zT$ value in the above example were to increase to 2 (with no changes in the optical or absorber efficiencies), a path towards generator efficiencies of 25% can be envisioned.

## Appendix: derivation of $\kappa_{eff}$

### Introduction

Modeling heat transport within thermoelectric materials requires consideration of not just the Fourier heat conduction, but also the Peltier and Thomson effects. Rather than considering each of these effects separately, we derive an "effective thermal conductivity" ($\kappa_{eff}$), which allows us to model the thermoelectric material as if Fourier conduction were the only heat transfer mechanism. The final expression for $\kappa_{eff}$ encompasses the traditional Fourier heat conduction, but also the heat generation/consumption due to the Peltier and Thomson effects.

In this model, we consider an optimized thermoelectric generator (TEG) using thermoelectric compatibility theory (for a detailed derivation, see ref. 45). We assume that the reduced current density ($u$) is equal to the thermoelectric compatibility factor ($s$) across the entire TE leg. We allow the Seebeck coefficient ($\alpha$) and the resistivity ($\rho$) to vary with temperature, but the thermal conductivity ($\kappa$) and the $zT$ value are assumed to be constant.

### Heat flux expressions

The total heat flux ($Q$) through a TE at any point in the leg can be written in terms of the current density ($J$) and the thermoelectric potential ($\Phi$) as:

$$Q = J\Phi \tag{A.1}$$

This equation includes both the Peltier and the Fourier heats. We can also write the heat flux in terms of $u$. Because we are interested in the heat flux into the TE at the hot side ($Q_h$), we write the reduced form of eqn (A.1) specifically for this flux by means of the scaling integral:[46]



 

$$Q_h = \frac{\Phi_h \int_{T_c}^{T_h} \kappa u \mathrm{d}T}{l} \quad (A.2)$$

We wish to express the heat flux in terms of an effective $\kappa$ that describes the heat flux into the TE at $T_h$. This effective term is expressed by eqn (A.3). Note that this $\kappa_{eff}$ will be different than the $\kappa_{eff}$ derived to describe the $Q$ leaving the leg on the cold side. For this reason, we will denote $\kappa_{eff}$ as $\kappa_{eff,h}$ in the following derivation.

$$Q_h = \frac{\kappa_{eff,h}}{l}(T_h - T_c) \quad (A.3)$$

Equating the two heat fluxes gives an expression for $\kappa_{eff,h}$:

$$\kappa_{eff,h} = \frac{\Phi_h}{(T_h - T_c)} \int_{T_c}^{T_h} \kappa u \mathrm{d}T \quad (A.4)$$

### Thermoelectric compatibility theory

From eqn (A.4), it is clear that we must consider $u(T)$. In order to simplify this task, let $u = s$ across the entire leg. For a thermoelectric generator, in a $u = s$ model,

$$u = s = \frac{\sqrt{1+zT} - 1}{\alpha T} \quad (A.5)$$

By substituting $s$ into eqn (A.4) and recalling that we have defined both $\kappa$ and $zT$ as constant with temperature, we have:

$$\kappa_{eff,h} = \frac{\kappa \Phi_h \left(\sqrt{1+zT} - 1\right)}{T_h - T_c} \int_{T_c}^{T_h} \frac{1}{\alpha T} \mathrm{d}T \quad (A.6)$$

We see that, in order to analytically solve for $\kappa_{eff,h}$, we will need an expression for $\alpha(T)$.

### Temperature dependence of $\alpha$

We begin by returning to the definition of $u$:

$$u = \frac{J}{\kappa \nabla T} \quad (A.7)$$

In this equation $u$ is a function of both $T$ and a spatial coordinate. By writing the heat balance equation in terms of $u$, we can eliminate any reference to the spatial coordinate:

$$\frac{\mathrm{d}u}{\mathrm{d}T} = u^2 T \frac{\mathrm{d}\alpha}{\mathrm{d}T} + u^3 \rho \kappa \quad (A.8)$$

In order to solve for $\alpha(T)$, we first rewrite eqn (A.8), recalling that $z = \frac{\alpha^2}{\rho\kappa}$:

$$\frac{\mathrm{d}}{\mathrm{d}T}\left(\frac{-1}{u}\right) = T \frac{\mathrm{d}\alpha}{\mathrm{d}T} + u \frac{\alpha^2}{z} \quad (A.9)$$

Also recall that $zT$ is a constant. To simplify, let $zT = k_o$, such that $z = k_o/T$. Substituting our definition of $s$ (see eqn (A.5)) into eqn (A.9) gives:

$$T \frac{\mathrm{d}\alpha}{\mathrm{d}T}\left[\frac{1}{1-\sqrt{1+k_o}} - 1\right] = \alpha\left[\frac{\sqrt{1+k_o}-1}{k_o} - \frac{1}{1-\sqrt{1+k_o}}\right] \quad (A.10)$$

To simplify, we define the parameters $k_1$ and $k_2$:

$$k_1 = \frac{\sqrt{1+k_o}-1}{k_o} - \frac{1}{1-\sqrt{1+k_o}}$$

$$k_2 = \frac{1}{1-\sqrt{1+k_o}} - 1$$

$$\frac{k_1}{k_2} = k_g = \frac{2 - 2\sqrt{1+k_o}}{k_o} \quad (A.11)$$

such that eqn (A.10) becomes:

$$\frac{\mathrm{d}\alpha}{\alpha} = k_g \frac{\mathrm{d}T}{T} \quad (A.12)$$

This can be solved to give an expression for $\alpha(T)$:

$$\alpha = \alpha_{ref}\left(\frac{T}{T_{ref}}\right)^{k_g} \quad (A.13)$$

Here, $\alpha_{ref}$ and $T_{ref}$ are simply reference values at any point along the leg.

### Returning to our expression for $\kappa_{eff,h}$

Substituting our definition of $\alpha(T)$ from eqn (A.13) into eqn (A.6), and removing constants from the integral gives:

$$\kappa_{eff,h} = \frac{\kappa \Phi_h \left(\sqrt{1+zT} - 1\right)}{T_h - T_c} \frac{T_{ref}^{k_g}}{\alpha_{ref}} \int_{T_c}^{T_h} T^{-(k_g+1)} \mathrm{d}T \quad (A.14)$$

As $k_g$ is a constant, the integral can be solved to give:

$$\kappa_{eff,h} = \frac{\kappa \Phi_h \left(\sqrt{1+zT} - 1\right)}{T_h - T_c} \frac{T_{ref}^{k_g}}{\alpha_{ref}} \left(\frac{-1}{k_g}\right)\left(T_h^{-k_g} - T_c^{-k_g}\right) \quad (A.15)$$

We can define $\Phi_h$ in terms of the temperature and the material properties:

$$\Phi_h = \alpha_h T_h + \frac{1}{u_h} \quad (A.16)$$

Again applying eqn (A.5) to replace $u$ with $s$ yields:

$$\Phi_h = \alpha_h T_h \left(\frac{\sqrt{1+zT}}{\sqrt{1+zT} - 1}\right) \quad (A.17)$$

This expression for $\Phi_h$ can be substituted into eqn (A.15) to give:

$$\kappa_{eff,h} = \frac{\kappa \alpha_h T_h \sqrt{1+zT}}{T_h - T_c} \left(\frac{-T_{ref}^{k_g}}{k_g\, \alpha_{ref}}\right)\left(T_h^{-k_g} - T_c^{-k_g}\right) \quad (A.18)$$

Lastly, we can evaluate our expression for $\alpha(T)$ (eqn (A.13)) at $T_h$ to give $\alpha_h$. Combining this with eqn (A.18) gives:

$$\kappa_{eff,h} = \frac{\kappa T_h \sqrt{1+zT}}{T_h - T_c} \alpha_{ref} \left(\frac{T_h}{T_{ref}}\right)^{k_g} \left(\frac{-T_{ref}^{k_g}}{k_g\, \alpha_{ref}}\right)\left(T_h^{-k_g} - T_c^{-k_g}\right) \quad (A.19)$$

We find that $\alpha_{ref}$ and $T_{ref}$ cancel, leaving us with a closed form expression that is solely dependent on our constants.

$$\kappa_{\mathrm{eff,h}} = \frac{\kappa T_{\mathrm{h}}\left(1+zT+\sqrt{1+zT}\right)}{2(T_{\mathrm{h}}-T_{\mathrm{c}})}\left(1-\left(\frac{T_{\mathrm{h}}}{T_{\mathrm{c}}}\right)^{k_{\mathrm{g}}}\right) \qquad (A.20)$$

$$k_{\mathrm{g}} = \frac{2-2\sqrt{1+zT}}{zT}$$

We can examine the dependence of $\kappa_{\mathrm{eff,h}}$ on $zT$ and $T_{\mathrm{h}}$ with the following plot:

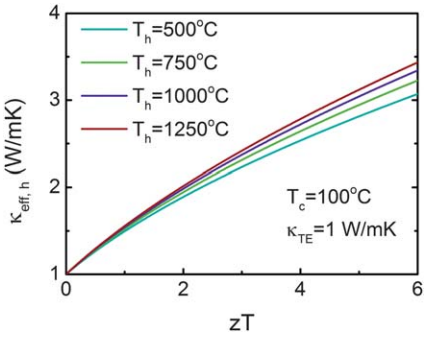


## Acknowledgements

LLB was supported by the Department of Defense (DoD) through the National Defense Science & Engineering Graduate Fellowship (NDSEG) Program. GJS gratefully acknowledges the support of the Jet Propulsion Laboratory. EST acknowledges the NSF Materials Research Science and Engineering Center at CSM (NSF-MRSEC award DMR0820518) for funding. We thank Andriy Zakutayev for his insights and discussion.

## References

1 R. Margolis, C. Coggeshall and J. Zuboy, *SunShot Vision Study*, U.S. Department of Energy, 2012.
2 G. J. Snyder and E. S. Toberer, Complex thermoelectric materials, *Nat. Mater.*, 2008, **7**, 105–114.
3 C. Wood, Materials for thermoelectric energy conversion, *Rep. Prog. Phys.*, 1988, **51**, 459–539.
4 A. J. Minnich, M. S. Dresselhaus, Z. F. Ren and G. Chen, Bulk nanostructured thermoelectric materials: current research and future prospects, *Energy Environ. Sci.*, 2009, **2**, 466–479.
5 C. J. Vineis, A. Shakouri, A. Majumdar and M. G. Kanatzidis, Nanostructured thermoelectrics: big efficiency gains from small features, *Adv. Mater.*, 2010, **22**, 3970–3980.
6 S. K. Bux, J.-P. Fleurial and R. B. Kaner, Nanostructured materials for thermoelectric applications, *Chem. Commun.*, 2010, **46**, 8311–8324.
7 E. S. Toberer, A. F. May and G. J. Snyder, Zintl chemistry for designing high efficiency thermoelectric materials, *Chem. Mater.*, 2010, **22**, 624–634.
8 T. Caillat, *et al.*, Progress Status of the Development of High-efficiency Segmented Thermoelectric Couples, *Nuclear and Emerging Technologies for Space*, 2012.
9 A. D. LaLonde, Y. Z. Pei and G. J. Snyder, Reevaluation of $PbTe_{1-x}I_x$ as high performance n-type thermoelectric material, *Energy Environ. Sci.*, 2011, **4**, 2090–2096.
10 R. H. Liu, *et al.*, p-Type skutterudites $R_xM_yFe_3CoSb_{12}$ (R, M = Ba, Ce, Nd, and Yb): effectiveness of double-filling for the lattice thermal conductivity reduction, *Intermetallics*, 2011, **19**, 1747–1751.
11 A. F. May, J. P. Fleurial and G. J. Snyder, Optimizing thermoelectric efficiency in $La_{3-x}Te_4$ *via* Yb substitution, *Chem. Mater.*, 2010, **22**, 2995–2999.
12 Y. Z. Pei, A. LaLonde, S. Iwanaga and G. J. Snyder, High thermoelectric figure of merit in heavy hole dominated PbTe, *Energy Environ. Sci.*, 2011, **4**, 2085–2089.
13 B. Poudel, *et al.*, High-thermoelectric performance of nanostructured bismuth antimony telluride bulk alloys, *Science*, 2008, **320**, 634–638.
14 X. Shi, *et al.*, Multiple-filled skutterudites: high thermoelectric figure of merit through separately optimizing electrical and thermal transports (vol 133, pg 7837, 2011), *J. Am. Chem. Soc.*, 2012, **134**, 2842.
15 X. A. Yan, *et al.*, Experimental studies on anisotropic thermoelectric properties and structures of n-type $Bi_2Te_{2.7}Se_{0.3}$, *Nano Lett.*, 2010, **10**, 3373–3378.
16 J. Paik, E. Brandon, T. Caillat, R. Ewell and J. Fleurial, Life Testing of $Yb_{14}MnSb_{11}$ for High Performance Thermoelectric Couples, *Proceedings of Nuclear and Emerging Technologies for Space*, 2011.
17 G. Chen, Theoretical efficiency of solar thermoelectric energy generators, *J. Appl. Phys.*, 2011, **109**, 104908.
18 G. Sala, D. Pachon and I. Anton, *Test, Rating and Specification of PV Concentrator Components and Systems: Classification of PV Concentrators*, Solar Energy Institute, Polytechnic University of Madrid., Madrid, Spain, 2002.
19 S. A. Kalogirou, Solar thermal collectors and applications, *Prog. Energy Combust. Sci.*, 2004, **30**, 231–295.
20 M. Garcia, L. Marroyo, E. Lorenzo and M. Perez, Soiling and other optical losses in solar-tracking PV plants in Navarra, *Prog. Photovoltaics*, 2010, **19**, 211–217.
21 N. P. Sergeant, O. Pincon, M. Agrawal and P. Peumans, Design of wide-angle solar-selective absorbers using aperiodic metal-dielectric stacks, *Opt. Express*, 2009, **17**, 22800–22812.
22 C. Kennedy, Review of mid-to high-temperature solar selective absorber materials, Report No. NREL/TP-520-32167, 2002.
23 M. K. Hedayati, *et al.*, Design of a perfect black absorber at visible frequencies using plasmonic metamaterials, *Adv. Mater.*, 2011, **23**, 5410.
24 C. H. Lin, R. L. Chern and H. Y. Lin, Polarization-independent broad-band nearly perfect absorbers in the visible regime, *Opt. Express*, 2011, **19**, 415–424.
25 H. Sai, H. Yugami, Y. Kanamori and K. Hane, Solar selective absorbers based on two-dimensional W surface gratings with submicron periods for high-temperature photothermal conversion, *Sol. Energy Mater. Sol. Cells*, 2003, **79**, 35–49.
26 E. Weston, Apparatus for utilizing solar radiant energy, 1888, Patent No. 389, 124.
27 E. Weston, Art of utilizing solar radiant energy, 1888, Patent No. 389, 125.
28 M. L. Severy, Apparatus for generating electricity by solar heat, 1894, Patent No. 527, 379.
29 M. L. Severy, Apparatus for mounting and operating thermopiles, 1894, Patent No. 527, 377.
30 W. W. Coblentz, Thermal generator, 1913, Patent No. 1077, 219.
31 M. Telkes, Solar thermoelectric generators, *J. Appl. Phys.*, 1954, **25**, 13.
32 D. Kraemer, *et al.*, High-performance flat-panel solar thermoelectric generators with high thermal concentration, *Nat. Mater.*, 2011, **10**, 532–538.
33 J. C. Chen, Thermodynamic analysis of a solar-driven thermoelectric generator, *J. Appl. Phys.*, 1996, **79**, 2717–2721.
34 S. A. Omer and D. G. Infield, Design optimization of thermoelectric devices for solar power generation, *Sol. Energy Mater. Sol. Cells*, 1998, **53**, 67–82.
35 K. Suleebka, High temperature solar thermoelectric generator, *Appl. Energy*, 1979, **5**, 53–59.
36 H. Scherrer, L. Vikhor, B. Lenoir, A. Dauscher and P. Poinas, Solar thermolectric generator based on skutterudites, *J. Power Sources*, 2003, **115**, 141–148.
37 R. Amatya and R. J. Ram, Solar thermoelectric generator for micropower applications, *J. Electron. Mater.*, 2010, **39**, 1735–1740.
38 A. Novikov, Improvement of the efficiency of a solar thermoelectric battery, *J. Eng. Phys. Thermophys.*, 2001, **74**, 6.
39 C. Suter, P. Tomes, A. Weidenkaff and A. Steinfeld, Heat transfer and geometrical analysis of thermoelectric converters driven by concentrated solar radiation, *Materials*, 2010, **3**, 2735–2752.
40 K. McEnaney, D. Kraemer, Z. F. Ren and G. Chen, Modeling of concentrating solar thermoelectric generators, *J. Appl. Phys.*, 2011, **110**.
41 P. W. Bridgman, Note on the principle of detailed balancing, *Phys. Rev.*, 1928, **31**.



 

42 R. G. Sheppard, D. Morgan, D. M. Mathes and D. J. Bray, *Properties and Characteristics of Graphite*, Poco Graphite, Inc., 2002.
43 H. J. Goldsmid, *Introduction to Thermoelectricity*, Springer-Verlag, 2010.
44 R. R. Heikes and R. W. Ure, *Thermoelectricity: Science and Engineering*, Interscience, New York, 1961.
45 G. J. Snyder, *Thermoelectric Power Generation: Efficiency and Compatibility*, CRC Press, Taylor & Francis Group, Boca Raton, FL, USA, 2006, ch. 9.
46 G. J. Snyder and T. S. Ursell, Thermoelectric efficiency and compatibility, *Phys. Rev. Lett.*, 2003, **91**.
47 W. T. Xie, Y. J. Dai, R. Z. Wang and K. Sumathy, Concentrated solar energy applications using fresnel lenses: a review, *Renew. Sustain. Energ. Rev.*, 2011, **15**, 2588–2606.
48 S. Kurtz, *Opportunities and Challenges for Development of a Mature Concentrating Photovoltaic Power Industry*, National Renewable Energy Laboratories, 2011.
49 M. Peters, *et al.*, Spectrally-selective photonic structures for PV applications, *Energies*, 2010, **3**, 171–193.
50 A. G. Imenes and D. R. Mills, Spectral beam splitting technology for increased conversion efficiency in solar concentrating systems: a review, *Sol. Energy Mater. Sol. Cells*, 2004, **84**, 19–69.
51 H. Hernandez-Noyola, D. H. Potterveld, R. J. Holt and S. B. Darling, Optimizing luminescent solar concentrator design, *Energy Environ. Sci.*, 2012, **5**, 5798–5802.
52 R. K. Kostuk and G. Rosenberg, Analysis and design of holographic solar concentrators, *Proc. Soc. Photo. Opt. Instrum. Eng.*, 2008, **7403**.
53 J. D. McCambridge, *et al.*, Compact spectrum splitting photovoltaic module with high efficiency, *Prog. Photovoltaics*, 2010, **19**, 352–360.
54 S. Ruehle, *et al.*, A two junction, four terminal photovoltaic device for enhanced light to electric power conversion using a low-cost dichroic mirror, *Renewable Sustainable Energy Rev.*, 2009, **1**.
55 J. Hernandez-Moro and J. M. Martinez-Duart, CSP electricity cost evolution and grid parities based on IEA roadmaps, *Energy Policy*, 2012, **41**, 184–192.
56 K. Branker, M. J. M. Pathak and J. M. Pearce, A review of solar photovoltaic levelized cost of electricity, *Renewable Sustainable Energy Rev.*, 2011, **15**, 4470–4482.